Synthesis and properties of rare-earth high-entropy perovskite

Rubayet Tanveer^{1, a)}, Dylan Windsor¹, Sean Drewry¹, Katharine Page^{1,2}, Haixuan Xu¹, Veerle Keppens^{1, a)}, and William J. Weber^{1, a)}

a) Author to whom correspondence should be addressed: rtanveer@vols.utk.edu, vkeppens@utk.edu, wjweber@utk.edu

ABSTRACT

The high entropy concept was applied to synthesize a set of rare-earth perovskites REBO₃ (RE=La, Pr, Nd, Sm, Eu, Gd) with the B-site occupied by Sc, Al, Cr, Ni, and Fe in equimolar ratios. All samples crystallize in the orthorhombic *Pnma* space group. Using an extended set of characterization measurements, the effects of multi-component material design and rare earth selection on the electronic properties are explored. Transport measurements show semiconducting behavior. PrBO₃, SmBO₃, and LaBO₃ show low-temperature magnetic ordering, with the ordering temperature shifting with the moment on the A-site.

The stabilization of a single crystalline phase using the concept of "high configurational entropy," with five or more cations on a specific lattice site was first demonstrated by *Rost et al.* who introduced 5 different cations on the Mg cation site in rocksalt MgO ¹. Following this work, many other research groups were able to synthesize complex high-entropy structures, including perovskites, pyrochlores, and spinels. ²⁻⁵. Populating a single lattice site with distinct elemental cations, often with significantly different ionic radii, brings about a built-in disorder and opens a way for property engineering.

In the present study, we apply the high entropy concept to a set of rare-earth perovskites to evaluate the tunability of the electronic and magnetic properties. The perovskite structure ABO₃ is known to lend itself to careful control of various properties via manipulation of the octahedral distortion ⁶⁻⁸. Both electronic and magnetic properties in this structure can be modified by changing the O-B bond length ⁹ and B-O-B bond angle ^{7,10}. For electronic properties, the bond geometry can regulate carrier mobility and band gap ^{7,9}. For magnetic properties, depending on the magnetic cation on the B-site, a 120°-180° B-O-B bond angle will favor antiferromagnetic super-exchange. In contrast, a 90° bond angle will favor ferromagnetic interaction ^{10,11}. Therefore, controlled exploitation of the bond geometry using high configurational disorder in high-entropy perovskites is expected to be important for device-applications, including spintronics ¹², memristors ¹³, voltage-gated magnetization ¹⁴, polar magnetics ¹⁵, and magneto-calories ^{16,17}. Hence, we selected a set of perovskites RE(ScCrFeNiAl)O₃ (Acronym: RESCFNA), with a rare-earth cation (RE =

¹Department of Materials Science and Engineering, The University of Tennessee Knoxville, Knoxville, Tennessee 37996, USA.

²Neutron Scattering Division, Oak Ridge National Laboratory, Oak Ridge, Tennessee 37830, USA.

La³⁺, Pr³⁺, Nd³⁺, Sm³⁺, Eu³⁺, Gd³⁺) on the A-site and *3d* transition metals in equimolar ratio on the B-site. B-cations of choice are Cr³⁺, Fe³⁺, and Ni³⁺, along with Sc³⁺ and Al³⁺. The large ionic radius ¹⁸ of Sc³⁺ should distort the B-O-B bond angle from 180°, creating a well-defined band gap ^{19,20}. Al³⁺ was also added to the B-site, along with the remaining three cations to bring the Goldschmidt tolerance factor closer to '1' ^{21,22}. Al³⁺ is also expected to bring the B-O-B bond angle close to 180° and decrease the length of the O-B bond. As a result, it enhances electronic conduction even though it does not contribute any conduction electron.

99.9% pure La₂O₃, Pr₂O₃, Nd₂O₃, Sm₂O₃, Eu₂O₃, Gd₂O₃, Sc₂O₃, Cr₂O₃, Fe₂O₃, NiO, Al₂O₃ powders (Sigma Aldrich and Alfa Aesar) were mixed stoichiometrically. Each mixture was ball milled in five-gram batches for 2 hours in a SPEX 8000M Mixer/Mill. The samples were then ground using an agate mortar and pestle to make the mixture more homogenous. The powders were subsequently compressed into a compact pellet and sintered for 10 hours at 1500 °C in a high-temperature MTI box furnace. To achieve single-phase powders, the grinding and sintering process was repeated at least three times (five times for the 11-cation composition).

To acquire high-density samples, the single-phase powders were hot-pressed using a uniaxial hot press at 1500 °C and 37.5 MPa under flowing argon to reduce vaporization. The samples were subsequently air-annealed in the MTI box furnace for ten hours at 1500 °C to reduce residual stress and remove carbon from the sample surface.

The PANalytical Empyrean multipurpose diffractometer was used to collect data on the specimens at 0.04-radian steps per min for 2θ from $10\text{-}90^\circ$ using CuK α_1 radiation (λ = 1.54051 Å) with Bragg-Brentano geometry. Lattice parameters were determined from a Rietveld refinement analysis using the HighScore Plus software with R_{wp} 10% or less. To verify site concentration homogeneity and sample composition purity, energy dispersive X-ray spectroscopy (EDS) with mapping was carried out using a Zeiss EVO microscope at a voltage of 15 kV down to 10KX magnification.

A four-probe technique was used to measure the electrical resistance of the samples with known dimensions (3 - 5 mm long and 0.5 -1 mm width and thickness) as a function of temperature at zero applied magnetic field between 300 K to 2 K using a Quantum Design Dynacool multipurpose physical property measurement system (PPMS). A current from 1000-5000 μ A was used to excite the sample.

Magnetization (M) versus Temperature (T) data was collected using a Quantum Design MPMS3 Superconducting Quantum Interference Device (SQUID) magnetometer. The specimen was cooled down to 2 K in a zero magnetic field (ZFC). For field cooling, an external magnetic field of up to 5 Tesla was applied during cooling (FC). Afterward, at μ_0H =0.1 Tesla both ZFC and FC magnetization data were recorded. The magnetization at room temperature (300 K) was determined for different applied fields ranging from μ_0H = 0 to 7 Tesla.

Heat capacity was measured in a PPMS under ultra-high vacuum (few mTorr). An addendum measurement was first run with N-grease. The sample with known mass was subsequently placed on the N-grease and the measurement was repeated.

Density functional theory (DFT) simulations were performed in Vienna *ab initio* simulations package (VASP) ^{23,24} using the PBEsol functional ²⁵. A Hubbard-U correction (DFT+U) ²⁶ was applied to obtain the relaxed structures and electronic structure. All supercells of 200 atoms were generated using special quasi-random structures (SQSs) ²⁷ within the ATAT toolkit ²⁸⁻³¹. A gamma-point calculation was used for computational efficiency with an energy cutoff of 550 eV. The pseudopotentials used in this study are in the planar-augmented wave (PAW) basis ³²: A-sites: Pr *5p4f6s* (11 e⁻), and Sm *5p4f6s* (11 e⁻) – B-sites: Al *2s2p* (3 e⁻), Sc *3s3p3d4s* (11 e⁻), Cr *3p3d4s* (12 e⁻), Fe *3p3d4s* (14 e⁻), Ni *3p3d4s* (16 e⁻) – O *2s2p* (6 e⁻). All calculations were converged to a total energy difference of <10⁻⁶ eV and each relaxation was converged to Hellmann-Feynman forces of <0.01 eV/Å.

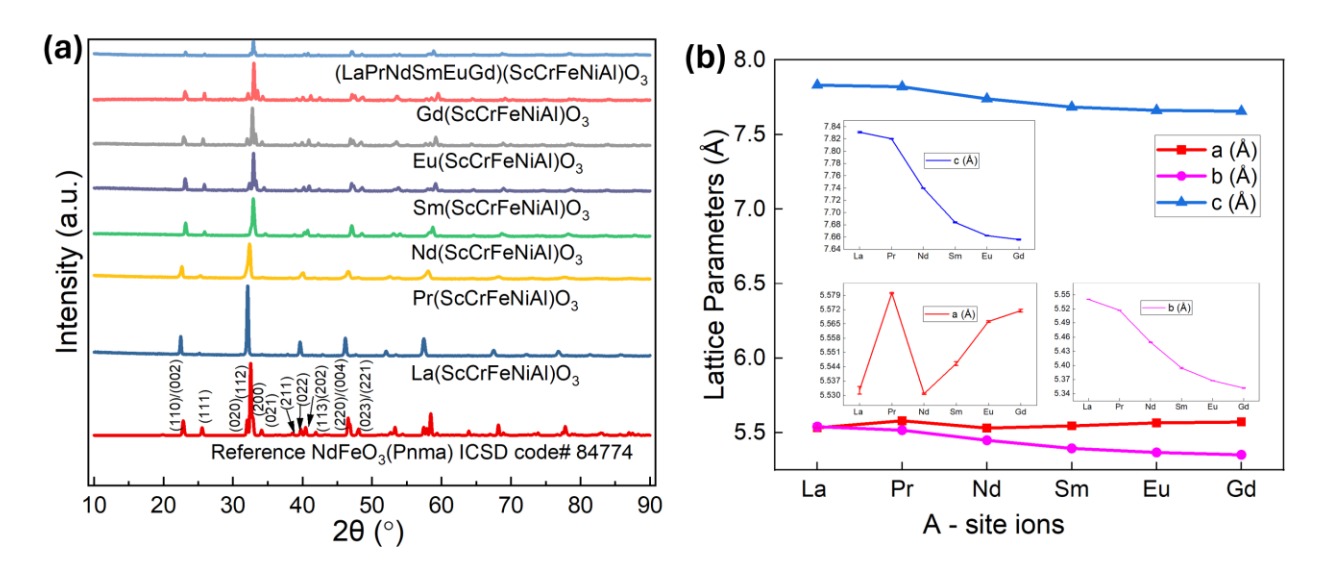


FIG. 1. (a) X-ray diffraction patterns of RE(ScCrFeNiAl)O₃ perovskites showing orthorhombic Pnma type structure with a reference NdFeO₃ pattern ³³. (b) Lattice parameters vs A-site cations.

Figure 1(a) provides x-ray diffraction patterns of synthesized RE(ScCrFeNiAl)O₃ with RE= La to Gd, along with the 11-cation composition. All compounds crystallize in the orthoferrite/orthochromite Pnma-type orthorhombic structure. No peaks from secondary phases were observed. These results closely match previously reported orthorhombic high entropy perovskites 3,34 . Several diffraction peaks show splitting as we move from La to Gd, i.e. with decreasing rare-earth ionic radii – a general trend with 'lanthanide contraction' as the structure turning towards lower symmetry. In addition, Rietveld refined lattice parameters in show that the difference between lattice parameters a and b increases while lattice parameter c decreases continuously with decreasing ionic radii of the A-site rare earths (Figure 1(b)) (see supplementary table 1 for lattice parameter values).

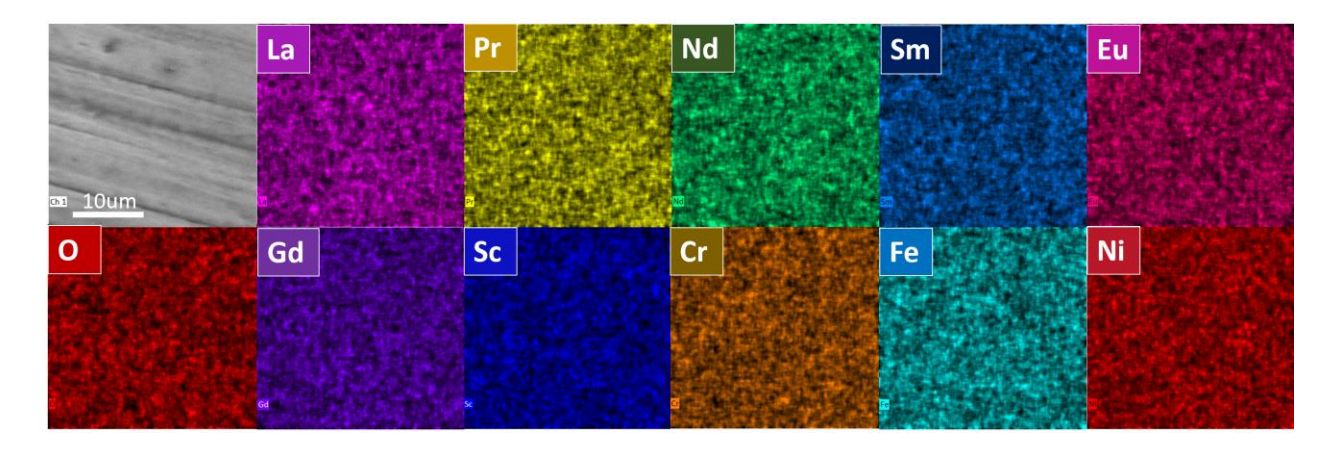


FIG. 2. Surface energy dispersive spectroscopy (EDS) mapping of 11-cation (LaPrNdSmEuGd)(ScCrFeNiAl)O₃ perovskite showing the homogeneous distribution of cations.

Surface EDS mapping was performed to investigate the homogeneous mixing of the cations for the 11-cation compound. All single cations are homogeneously distributed across the imaged surface at the tens of microns length-scale and no clustering is observed.

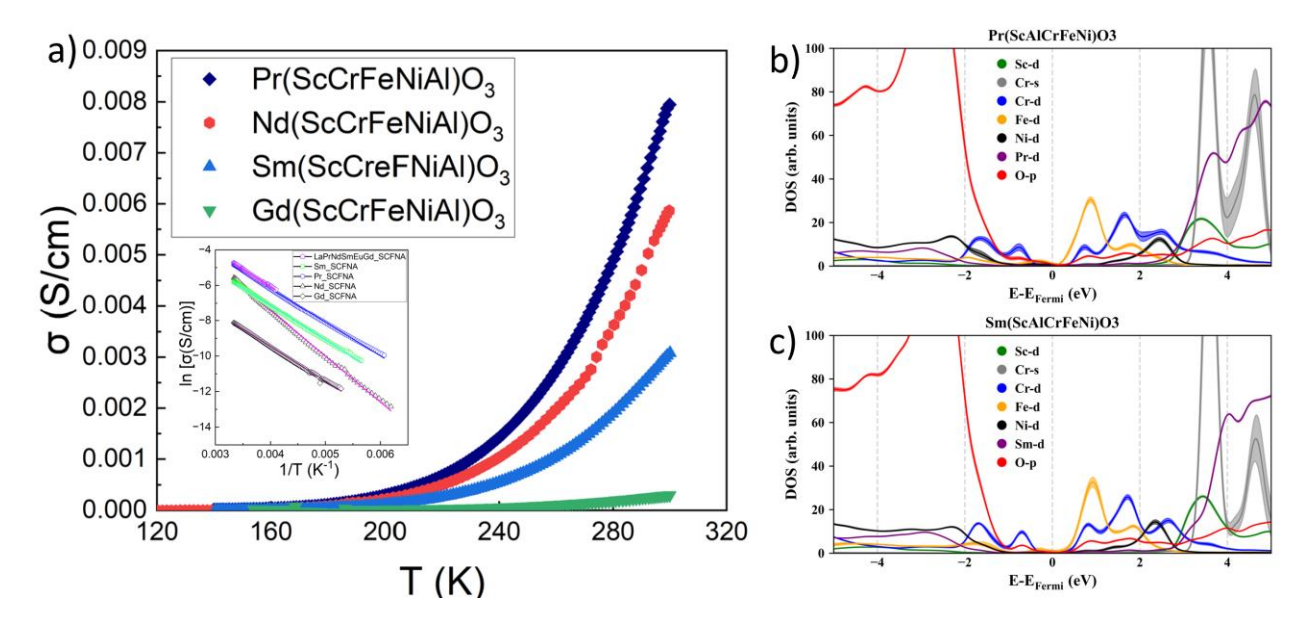


FIG. 3. (a) Electrical conductivity vs Temperature showing the intrinsic region and its exponential rise in conductivity for samples with Pr, Nd, Sm, or Gd on the A-site andArrhenius plot of the natural log of the conductivity vs 1/*T* for the same region (inset) (left). Calculated density of states (DOS) for (b) Pr(ScCrFeNiAl)O₃ and (c) Sm(ScCrFeNiAl)O₃ (right).

Figure 3 displays the electrical conductivity for several A-site rare earth high entropy (HE) perovskites as a function of temperature, from 120 K to 300 K (the corresponding intrinsic area).

The increase in conductivity with temperature follows an exponential trend, as evidenced by the straight-line behavior in the insets, indicating that these compounds behave like elemental semiconductors (see Supplementary Fig. 1 for an extended temperature range). Also, we observe an increase in conductivity with increasing ionic radii of the rare earth A-site, which is discussed in the following section. The room temperature values of conductivity are $0.008 \, (\pm \, 0.0005)$, $0.006 \, (\pm \, 0.0005)$, $0.0031 \, (\pm \, 0.0002)$, and $0.0003 \, (\pm \, 0.00002)$ S/cm for Pr, Nd, Sm, and Gd samples respectively. These values are comparable to recent studies on HE perovskites with different B-sites (the authors used Mn and Co instead of Sc and Al) 34,35 . Considering the exponential behavior in the intrinsic region, we fitted the conductivity with the following Arrhenius equation,

$$\sigma = \sigma_0 \cdot e^{-\frac{E_g}{2kT}}$$

The energy gap parameter, E_g ranges from 0.32 eV to 0.34 eV depending on the rare earth on the A-sites (Table II). This is analogous with previous studies, indicating that changing the rare earth on the A site while keeping the B-site constant, does not change the band gap drastically $^{36-38}$.

TABLE I. Band gap comparison between HE and single B-atom perovskites.

Perovskites	Experimental Band Gap (eV)	Computational Band Gap (eV)	References
PrScO ₃	5.7	5.7	37
PrCrO ₃	3.2	2.7	39,40
PrFeO ₃	3.39	3.22	41
PrAlO ₃	4.59	3.8	38,42
PrNiO ₃	1	0.74	9,19
Pr(Fe _{0.5} Ni _{0.5})O ₃	0.118	-	43
Pr(ScCrFeNiAl)O ₃	0.32 ± 0.001 (Arrhenius fit)	No gap	Present Work
Nd(ScCrFeNiAl)O ₃	0.323 ± 0.001 (Arrhenius fit)	-	Present Work
Sm(ScCrFeNiAl)O ₃	0.335 ± 0.001 (Arrhenius fit)	0.01	Present Work
Gd(ScCrFeNiAl)O ₃	0.336 ± 0.001 (Arrhenius fit)	-	Present Work
(LaPrNdSmEuGd)(Sc CrFeNiAl)O ₃	0.34 ± 0.001 (Arrhenius fit)	-	Present Work

Table I provides a band gap comparison with perovskites with single B-site transition metals while keeping the A-site fixed (with Pr). Interestingly, except PrNiO₃, which exhibits an experimental charge transfer energy of 1 eV (still, significantly greater) than the cumulative B-site high entropy Pr(ScCrFeNiAl)O₃, all single B perovskites exhibit insulator-like behavior with a band gap of 3 eV and above. One earlier study demonstrated that Ni inclusion can lower the gap value of PrFeO₃ to as much as 0.118 eV ⁴³. The comparatively low energy gap in PrNiO₃ is due to the combination of strong hybridization between low spin Ni³⁺ $3d^7$ and O 2p orbitals along with orthoferrite-type distortion (the latter widens the gap) ^{19,44}. In Pr(Fe_{0.5}Ni_{0.5})O₃ disorder-induced localization and 3d band contraction play a critical role where gap lowering is due to hybridization of both Ni³⁺ 3d – O -2p (lower band) and Fe³⁺ 3d O-2p (higher band). Moreover, the coexistence of Ni³⁺ $(t^6 e^l)$ and $t^5 e^2$ increases the carrier concentration ⁴³.

The experimental data shown in Figure 3 indicates that the transport properties of our samples are more like an elemental semiconductor at its intrinsic region. Figure 3(b) and 3(c) shows density of states (DOS) calculations for a PrSCFNA and SmSCFNA sample. Both compounds show gaps or pseudo-gaps developing near the Fermi energy, but the DOS at the Fermi level for the PrSCFNA is slightly higher than the SmSCFNA, which matches the trend of our experimental findings.

Both this gap widening and decreasing conductivity trend is a consequence of the reduction in the ionic radii or 'Lanthanide contraction'. As the A site changes from Pr to Gd, the tolerance factor t $= (r_A + r_o)/\sqrt{2(r_B + r_o)}$ of the structures deviates further from the ideal value of 1. Such deviation impacts the O-B bond length with compressive stress ^{7,9} and reduces the B-O-B bond angle away from 180 degrees ⁷, thus inducing structural distortion (band gap widening) and inhibiting (B) 3d-2p (O) hopping (restricting carrier mobility) 9,45 . Following the same argument, it can be predicted that Sc on the B-site contributes to bandgap widening with its comparatively high ionic radius. Removing Sc from the B-site is therefore expected to promote metallic character. Figure 3(b) and (c) show the contributions from each separate band from -5eV to 5eV with the Fermi level E_F at 0 eV of PrSCFNA and SmSCFNA. Line expansions denote calculation errors. The calculations show that the electronic structure below E_F near the valence band maximum is dominated by Cr-3d and O-2p states with Ni-3d and Fe-3d contribution, and the conduction band (above E_F) is dominated by the contributions from mostly Fe-3d with Cr-3d, Ni-3d, and O-2p bands. Future X-ray absorption spectroscopy and/or Mössbauer spectroscopy measurements may reveal in-depth information about the 3d-2p or 3d-3d hybridization, crystal field splitting, Jahn-Teller distortions, and Ni^{2+}/Ni^{3+} concentration of such high-degree structurally disordered structures.

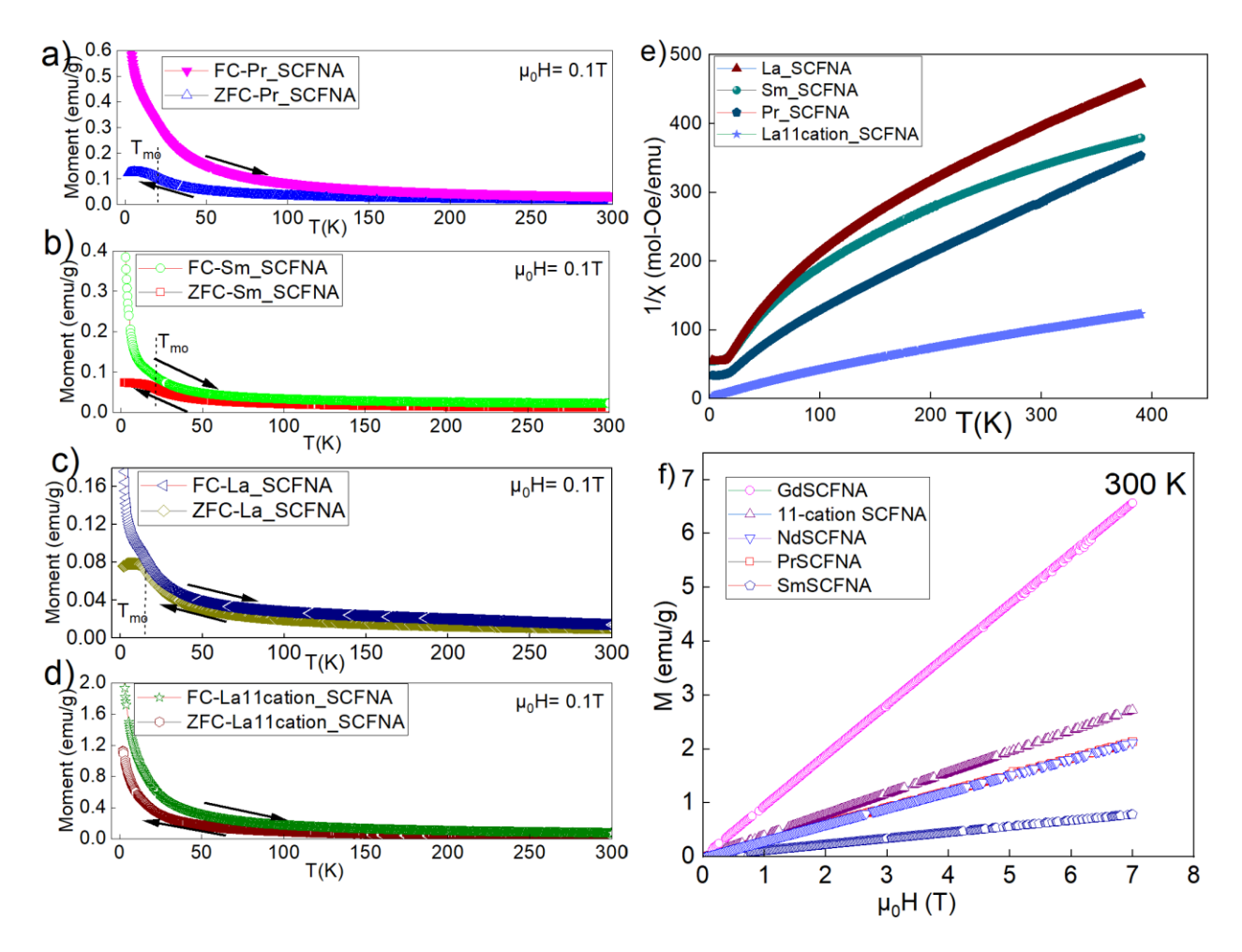


FIG. 4. DC magnetic moment vs Temperature for (a) Pr(ScCrFeNiAl)O₃, (b) Sm(ScCrFeNiAl)O₃, (c) La(ScCrFeNiAl)O₃, (d) (LaPrNdSmEuGd)(ScCrFeNiAl)O₃ at μ_0H = 0.1T. FC data were taken during cooling and ZFC were taken during warming. (e) Comparative curves for inverse susceptibility vs Temperature for the same samples. (f) Moment vs magnetic field from 0 to 7 Tesla at room temperature (300K).

Figure 4(a)-(d) shows the magnetic moment vs. temperature (measured at $\mu_0H = 0.1T$) for PrSCFNA, SmSCFNA, LaSCFNA, and the 11-cation perovskite (see supplementary Fig. 2 for NdSCFNA and GdSCFNA). There is a noticeable disparity between ZFC and FC data. We designate these deflection points as a magnetic ordering temperature (T_{mo}), which for LaSCFNA, SmSCFNA, and PrSCFNA is 16.8K, 18.3K, and 20.8K, respectively. Interestingly, the FC moment rises sharply below the ordering temperature whereas the ZFC moment remains constant or decreases. This substantiates that not all the moments participate in this low-temperature ordering and there are more than one coexisting magnetic phases, such as spin-glass coexisting with short-range ferro and antiferromagnetism 46,47 . None of our samples show magnetic ordering at higher (above 150 K) temperatures, in contrast with single cation REMO₃, like LaCrO₃, LaNiO₃, and LaFeO₃, which show ferromagnetic or antiferromagnetic ordering due to ordering of the B-site

transition metals ⁴⁸⁻⁵¹. The lack of high-temperature ordering in our materials can be a consequence of high configurational entropy effects like non-magnetic chemical disorder, weakly connected magnetic ions and their interrupted periodicity, dilution of magnetic ions, and competing interactions ^{52,53}. Figure 4(e) displays the inverse susceptibility vs. temperature, used to examine Curie-Weiss behavior. Our HE Perovskites with La, Pr, or Sm on the A-site show a deviation from the Curie-Weiss behavior at low temperatures. As we increase the configurational entropy by incorporating 6-rare earth on the A site, this deviation becomes much less pronounced. The observed curvature of the Curie-Weiss plots is likely due to a temperature-independent term in the susceptibility ⁵⁴. Figure 4(f) shows the room temperature magnetization versus the applied field (up to 7 T) for each material. Up to the maximum applied field, none of the three samples saturates. GdSCFNA shows the highest magnetization due to Gd³⁺ and the 11-cation perovskite shows the second highest magnetization due to Gd³⁺ and Nd³⁺ cations on the A-site.

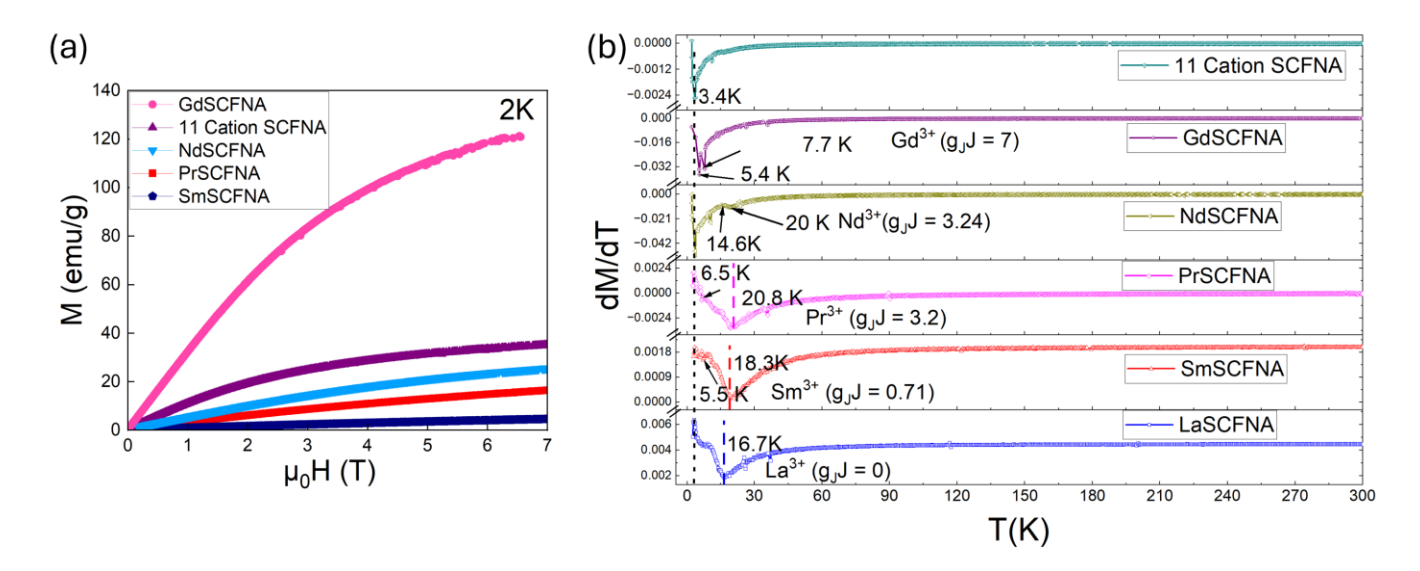


FIG. 5. (a) Low temperature (2 K) magnetic moment vs magnetic field (up to 7 Tesla). (b) Derivative of the Magnetic Moment vs Temperature for SmSCFNA, PrSCFNA, and LaSCFNA.

Figure 5(a) demonstrates that at low temperatures, the samples transition from being speromagnetic (SmSFCNA, PrSCFNA) to asperomagnetic (NdSCFNA, 11-cation SCFNA) and sperimagnetic as the A-moment increases, eventually converging saturation (GdSCFNA) ^{46,55}. The temperature-dependence of the derivative magnetic moment reveals more clearly the magnetic ordering temperatures of the Sm (18.3 K), Pr (20.8 K), and La (16.7 K) perovskites. Given the similar qualitative behavior, with similar ordering temperatures, it is expected that the origin of the transition is due to the B-site cation interactions. As La³⁺ has a total angular momentum value *J*=0, the transition for LaSCFNA is solely due to the ordering of B-site magnetic cations Ni³⁺, Cr³⁺, and Fe³⁺. As none of the single B perovskite (LaNiO₃, LaCrO₃, LaFeO₃) has magnetic ordering at low temperatures ^{49,50,56}, we assume it is caused by a super-exchange interaction between any two or all three of the magnetic B cations. Another B-site-driven short-range magnetic can be observed at 3.4 K, although there is no deflection at the *M-T* curves. It is interesting that the ordering

temperature increases with the gJ value or A-site moment and its magnitude starts disappearing from Nd³⁺ indicating the moment-dependent tunability of the ordering temperature (Figure 5(b)).

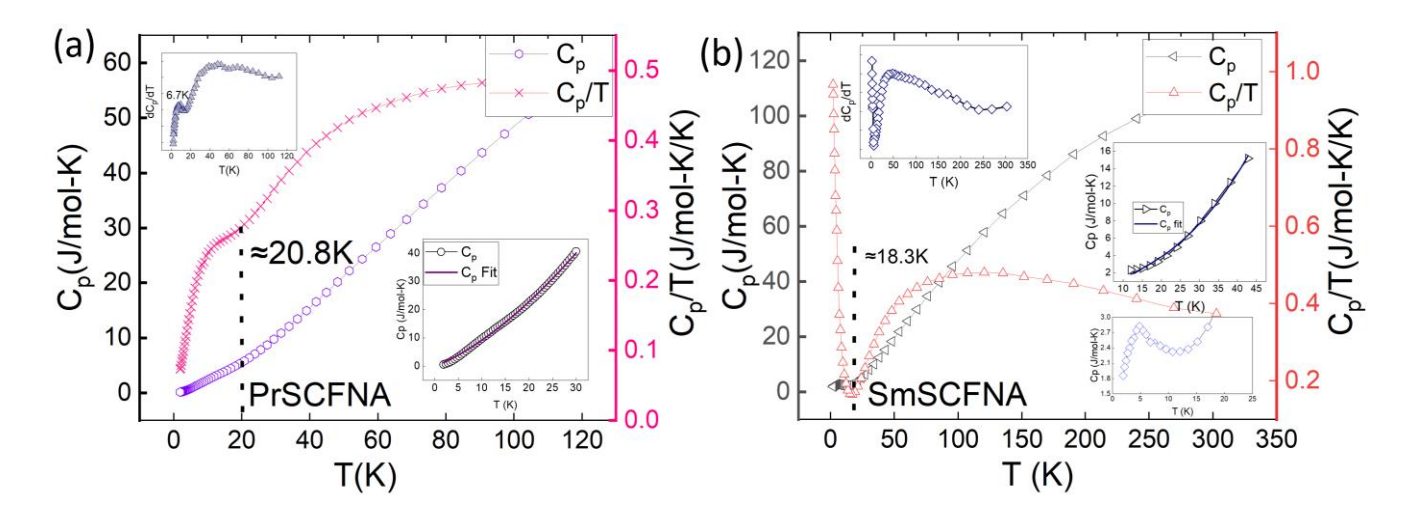


FIG. 6. Heat Capacity (C_p) vs Temperature and C_p/T vs Temperature for (a) PrSCFNA and (b) SmSCFNA. Inserts show dC_p/dT vs Temperature and a fit to the low-temperature C_p data.

Heat capacity (C_p) vs Temperature measurements were conducted at zero field to help identify the magnetic ordering temperatures. The absence of any sharp C_p peak or 'lambda anomaly' at T_{mo} with C_p/T vs T showing broad anomaly for both Pr and Sm perovskites near ~20.8 K and ~18.3 K respectively suggests spin glass ordering 46,57 . dC_p/dT vs Temperature for PrSCFNA shows a cusp at 6.7 K, while the data for SmSCFNA show a dent at 4.8 K (with C_p showing a peak at the same Temperature). Earlier work has shown that PrFeO₃ goes through a spontaneous spin reorientation at ~6.5 K and SmFeO₃ adopts a cooling-induced magnetization reversal below ~5 K 17,58 . The Low-temperature heat capacity data have been fitted with the following equation 48,59,60 ,

$$C_{\rm p} = \gamma T + \beta T^3 + \delta T^{3/2}$$

The fitted curves in Figure 6 use electronic parameter γ = 0.46 J/mol-K² and 0.086 J/mol-K² for PrSCFNA and SmSCFNA respectively – denotes higher DOS at the fermi level of the Pr sample compared to Sm – analogous with the calculations. The fit also allows us to evaluate the lattice contribution β = 1.1746 x 10⁻⁴ and 9.7658 x 10⁻⁵ J/mol-K⁴ and magnetic contribution δ = 0.1393 and 0.01478 J/mol-K^{3/2} for PrSCFNA and SmSCFNA. The lattice vibration contribution is related to the Debye Temperature (θ D) as, β = 234N k_{β}/θ_{D}^{3} (where N= no of ions per mole) and yields a relatively low Debye temperature of 255 K and 271 K for Pr and Sm perovskites, respectively, which is an indication of low thermal conductivity. The current group of samples was designed with a large variance in cationic radii on the B-site (Sc- 0.885Å, to Al- 0.675Å) ¹⁸ to induce more disorder and therefore more phonon scattering.

In summary, using the high entropy concept, we synthesized a set of polycrystalline rare-earth-based perovskite materials and evaluated the bulk structural, electronic, and magnetic properties. All samples show Arrhenius-like electronic conductivity at the intrinsic region. Low-temperature magnetic ordering is observed in PrBO₃, SmBO₃, and LaBO₃ (with B=(Sc_{1/5}Al/₁₅Cr_{1/5}Ni_{1/5}Fe_{1/5})). The flexibility to accommodate different rare earths and disparate B-site cations in the orthorhombic perovskite structure opens the opportunity to engineer the properties.

See supplementary material in which Supplementary Table I (S1) provides all the lattice parameters with HighScore Plus refined error bars. Supplementary Figure 1 (SF1) provides electrical transport data with cooling and warming and extended temperature range for selected samples. Supplementary Figure 2 (SF2) provides magnetic moment vs temperature data for additional samples.

This work was supported by the National Science Foundation under Grant No. DMR-2104228. Computational calculations (D.W. and H.X) were partially supported by the National Science Foundation Materials Research Science and Engineering Center program through the UT Knoxville Center for Advanced Materials and Manufacturing (DMR-2309083). XRD and EDS were performed at the Institute for Advanced Materials & Manufacturing (IAMM) Diffraction Facility and Microscopy Core, located at the University of Tennessee, Knoxville. Special thanks to William R. Meier, Seung-Hwan Do, and Shirin Mozaffari for the informative conversations on magnetic properties.

REFERENCES

- C. M. Rost, E. Sachet, T. Borman, A. Moballegh, E. C. Dickey, D. Hou, J. L. Jones, S. Curtarolo, and J.-P. Maria, Nature communications **6**, 8485 (2015).
- S. Jiang, T. Hu, J. Gild, N. Zhou, J. Nie, M. Qin, T. Harrington, K. Vecchio, and J. Luo, Scripta Materialia **142**, 116 (2018).
- A. Sarkar, R. Djenadic, D. Wang, C. Hein, R. Kautenburger, O. Clemens, and H. Hahn, Journal of the European Ceramic Society **38**, 2318 (2018).
- B. Musicó, Q. Wright, T. Z. Ward, A. Grutter, E. Arenholz, D. Gilbert, D. Mandrus, and V. Keppens, Physical Review Materials **3**, 104416 (2019).
- ⁵ C. Kinsler-Fedon, Q. Zheng, Q. Huang, E. S. Choi, J. Yan, H. Zhou, D. Mandrus, and V. Keppens, Physical Review Materials **4**, 104411 (2020).
- G. G. Guzmán-Verri, R. T. Brierley, and P. B. Littlewood, Nature **576**, 429 (2019).
- J.-S. Zhou and J. Goodenough, Physical Review B **69**, 153105 (2004).
- R. J. Tilley, *Perovskites: structure-property relationships* (John Wiley & Sons, 2016).

- D. Sarma, N. Shanthi, and P. Mahadevan, Journal of Physics: Condensed Matter **6**, 10467 (1994).
- ¹⁰ J. B. Goodenough, Physical Review **164**, 785 (1967).
- ¹¹ J. B. Goodenough, Physical Review **171**, 466 (1968).
- M. Bibes and A. Barthelemy, IEEE transactions on electron devices **54**, 1003 (2007).
- H. Nili, S. Walia, S. Balendhran, D. B. Strukov, M. Bhaskaran, and S. Sriram, Advanced Functional Materials **24**, 6741 (2014).
- S. Ning, Q. Zhang, C. Occhialini, R. Comin, X. Zhong, and C. A. Ross, ACS nano 14, 8949 (2020).
- P. Mandal, M. Pitcher, J. Alaria, H. Niu, P. Borisov, P. Stamenov, J. Claridge, and M. Rosseinsky, Nature **525**, 363 (2015).
- A. Barman, S. Kar-Narayan, and D. Mukherjee, Advanced Materials Interfaces **6**, 1900291 (2019).
- E. Li, Z. Feng, B. Kang, J. Zhang, W. Ren, and S. Cao, Journal of Alloys and Compounds **811**, 152043 (2019).
- R. D. Shannon, Acta crystallographica section A: crystal physics, diffraction, theoretical and general crystallography **32**, 751 (1976).
- T. Mizokawa, A. Fujimori, T. Arima, Y. Tokura, N. Mōri, and J. Akimitsu, Physical Review B **52**, 13865 (1995).
- J.-S. Zhou, J. Goodenough, B. Dabrowski, P. Klamut, and Z. Bukowski, Physical review letters **84**, 526 (2000).
- V. Goldschmidt, Transactions of the Faraday Society **25**, 253 (1929).
- H. D. Megaw, Transactions of the Faraday Society **42**, A224 (1946).
- G. Kresse and J. Furthmüller, Computational Materials Science **6**, 15 (1996).
- G. Kresse and J. Furthmüller, Physical Review B **54**, 11169 (1996).
- J. P. Perdew, A. Ruzsinszky, G. I. Csonka, O. A. Vydrov, G. E. Scuseria, L. A. Constantin, X. Zhou, and K. Burke, Physical Review Letters 100, 136406 (2008).

- S. L. Dudarev, G. A. Botton, S. Y. Savrasov, C. J. Humphreys, and A. P. Sutton, Physical Review B **57**, 1505 (1998).
- A. Zunger, S. H. Wei, L. G. Ferreira, and J. E. Bernard, Physical Review Letters **65**, 353 (1990).
- ²⁸ A. Van De Walle, Calphad **33**, 266 (2009).
- ²⁹ A. Van De Walle, M. Asta, and G. Ceder, Calphad **26**, 539 (2002).
- A. van de Walle, P. Tiwary, M. de Jong, D. L. Olmsted, M. Asta, A. Dick, D. Shin, Y. Wang, L. Q. Chen, and Z. K. Liu, Calphad **42**, 13 (2013).
- A. V. D. Walle and M. Asta, Modelling and Simulation in Materials Science and Engineering **10**, 521 (2002).
- ³² P. E. Blöchl, Physical Review B **50**, 17953 (1994).
- H. Taguchi, Journal of Solid State Chemistry **131**, 108 (1997).
- V. Zhivulin, E. Trofimov, S. Gudkova, A. Y. Punda, A. Valiulina, A. Gavrilyak, O. Zaitseva, D. Tishkevich, T. Zubar, and Z. Sun, Ceramics International **48**, 9239 (2022).
- V. E. Zhivulin, E. A. Trofimov, S. A. Gudkova, I. Y. Pashkeev, A. Y. Punda, M. Gavrilyak, O. V. Zaitseva, S. V. Taskaev, F. V. Podgornov, and M. A. Darwish, Nanomaterials **11**, 1014 (2021).
- M. K. Warshi, V. Mishra, A. Sagdeo, V. Mishra, R. Kumar, and P. Sagdeo, Ceramics International 44, 8344 (2018).
- C. Derks, K. Kuepper, M. Raekers, A. Postnikov, R. Uecker, W. Yang, and M. Neumann, Physical Review B **86**, 155124 (2012).
- M. Gupta, O. V. Rambadey, and P. R. Sagdeo, Ceramics International **48**, 23072 (2022).
- R. Mguedla, A. B. J. Kharrat, M. Saadi, K. Khirouni, N. Chniba-Boudjada, and W. Boujelben, Journal of Alloys and Compounds **812**, 152130 (2020).
- M. Yaseen, H. Ambreen, J. Iqbal, A. Shahzad, R. Zahid, N. A. Kattan, S. M. Ramay, and A. Mahmood, Philosophical Magazine **100**, 3125 (2020).
- A. T. S. Sudandararaj, G. S. Kumar, M. Dhivya, R. Eithiraj, and I. S. Banu, Journal of Alloys and Compounds **817**, 152747 (2020).
- ⁴² A. P. Sakhya, D. Rai, A. Dutta, R. Thapa, and T. Sinha, RSC advances **6**, 59988 (2016).

- R. Kumar, R. Choudhary, M. Ikram, D. Shukla, S. Mollah, P. Thakur, K. Chae, B. Angadi, and W. Choi, Journal of Applied Physics **102** (2007).
- ⁴⁴ X. Xu, J. Peng, Z. Li, H. Ju, and R. Greene, Physical Review B **48**, 1112 (1993).
- J. Torrance, P. Lacorre, A. Nazzal, E. Ansaldo, and C. Niedermayer, Physical Review B **45**, 8209 (1992).
- J. M. Coey, *Magnetism and magnetic materials* (Cambridge university press, 2010).
- Y. Yin, F. Shi, G.-Q. Liu, X. Tan, J. Jiang, A. Tiwari, and B. Li, Applied Physics Letters **120** (2022).
- S. Kumar, I. Coondoo, M. Vasundhara, S. Kumar, A. L. Kholkin, and N. Panwar, Journal of Physics: Condensed Matter **29**, 195802 (2017).
- B. Tiwari, A. Dixit, R. Naik, G. Lawes, and M. R. Rao, Materials Research Express 2, 026103 (2015).
- H. Guo, Z. Li, L. Zhao, Z. Hu, C. Chang, C.-Y. Kuo, W. Schmidt, A. Piovano, T. Pi, and O. Sobolev, Nature communications **9**, 43 (2018).
- A. Azad, A. Mellergård, S.-G. Eriksson, S. Ivanov, S. Yunus, F. Lindberg, G. Svensson, and R. Mathieu, Materials research bulletin **40**, 1633 (2005).
- J. Zhang, J. Yan, S. Calder, Q. Zheng, M. A. McGuire, D. L. Abernathy, Y. Ren, S. H. Lapidus, K. Page, and H. Zheng, Chemistry of Materials **31**, 3705 (2019).
- V. Zhivulin, E. Trofimov, O. Zaitseva, D. Sherstyuk, N. Cherkasova, S. Taskaev, D. Vinnik, Y. A. Alekhina, N. Perov, and D. Tishkevich, Ceramics International **49**, 1069 (2023).
- P. Dimitar, A. Bogdan, and L. Vasil, Journal of Rare Earths 28, 602 (2010).
- ⁵⁵ J. Coey, Journal of Applied Physics **49**, 1646 (1978).
- S. Acharya, J. Mondal, S. Ghosh, S. Roy, and P. Chakrabarti, Materials Letters **64**, 415 (2010).
- N. Lakshminarasimhan, A. N. Kumar, S. S. Chandrasekaran, and P. Murugan, Progress in Solid State Chemistry **54**, 20 (2019).
- ⁵⁸ J.-H. Lee, Y. K. Jeong, J. H. Park, M.-A. Oak, H. M. Jang, J. Y. Son, and J. F. Scott, Physical review letters **107**, 117201 (2011).
- B. F. Woodfield, M. L. Wilson, and J. M. Byers, Physical review letters **78**, 3201 (1997).

K. Sreedhar, J. Honig, M. Darwin, M. McElfresh, P. Shand, J. Xu, B. Crooker, and J. Spalek, Physical Review B **46**, 6382 (1992).

Synthesis and properties of rare-earth high-entropy perovskite

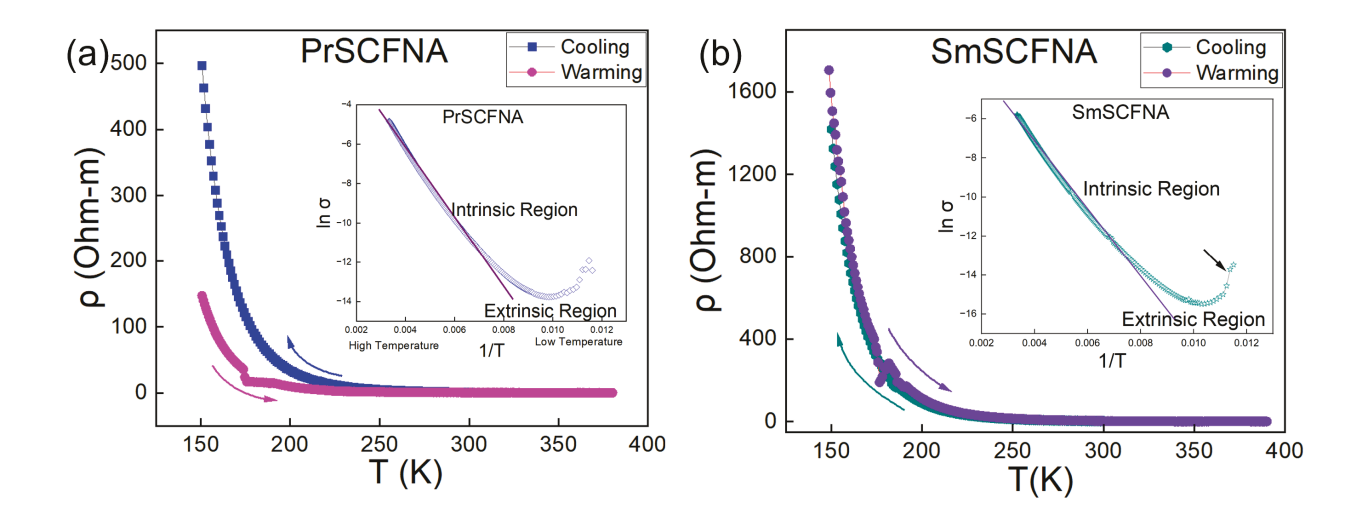
Rubayet Tanveer^{1, a)}, Dylan Windsor¹, Sean Drewry¹, Katharine Page^{1,2}, Haixuan Xu¹, Veerle Keppens^{1, a)}, and William J. Weber^{1, a)}

SUPPLEMENTARY TABLE I (S1). Rietveld refined lattice parameters of RE(ScCrFeNiAl)O $_3$ perovskites.

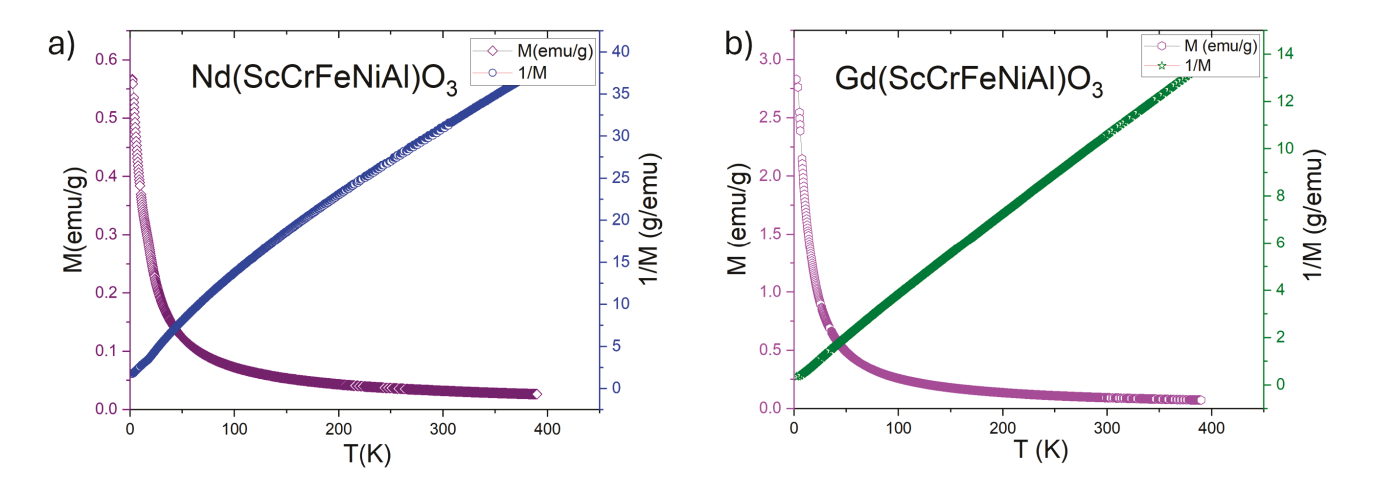
List of Compositions	Associated Phases	Lattice Parameters (Å)
La(ScCrFeNiAl)O ₂	Orthorhombic (Pnma)	$a = 5.5325 \pm 0.0019$
, , , ,	,	$b = 5.5399 \pm 0.0007$
		$c{=7.8309 \pm 0.0009}$
Pr(ScCrFeNiAl)O ₃	Orthorhombic (Pnma)	$a = 5.5801 \pm 0.0003$
J		$b = 5.5166 \pm 0.0003$
		$c = 7.8203 \pm 0.0004$
Nd(ScCrFeNiAl)O ₃	Orthorhombic (Pnma)	$a = 5.5308 \pm 0.0003$
, and the second		$b = 5.4491 \pm 0.0005$
		$c = 7.7397 \pm 0.0003$
Sm(ScCrFeNiAl)O ₃	Orthorhombic (Pnma)	$a = 5.5456 \pm 0.0009$
-		$b = 5.3944 \pm 0.0013$
		$c = 7.6838 \pm 0.0009$
Eu(ScCrFeNiAl)O ₃	Orthorhombic (Pnma)	$a = 5.5662 \pm 0.0004$
		$b = 5.3676 \pm 0.0004$
		$c = 7.6623 \pm 0.0006$
Gd(ScCrFeNiAl)O ₃	Orthorhombic (Pnma)	$a = 5.5715 \pm 0.0007$
		$b = 5.3521 \pm 0.0006$
		$c = 7.6560 \pm 0.0009$
(LaPrNdSmEuGd)(ScCrFeNiAl)O ₃	Orthorhombic (Pnma)	$a = 5.5352 \pm 0.00001$
•		$b = 5.4292 \pm 0.00001$
		$c = 7.7216 \pm 0.00001$

¹Department of Materials Science and Engineering, The University of Tennessee Knoxville, Knoxville, Tennessee 37996, USA.

²Neutron Scattering Division, Oak Ridge National Laboratory, Oak Ridge, Tennessee 37830, USA.



SUPPLEMENTARY FIG 1 (SF1). Cooling and warming data for electrical resistivity and their behavior at low temperature (inset) (a) PrSCFNA and (b) SmSCFNA.



SUPPLEMENTARY FIG 2 (SF2). Magnetic moment and inverse magnetic moment vs Temperature for (a) NdSCFNA and (b) GdSCFNA.